Thermally activated magnetization reversal in bulk $BiFe_{0.5}Mn_{0.5}O_3$

D. Delmonte,[1,*] F. Mezzadri,[2] C. Pernechele,[1] G. Calestani,[2,3] G. Spina,[4] M. Lantieri,[5] M. Solzi,[1] R. Cabassi,[2] F. Bolzoni,[2] A. Migliori,[6] C. Ritter,[7] and E. Gilioli[2]

[1]*Dipartimento di Fisica, Università di Parma, Parco Area delle Scienze 7/A, 43124 Parma, Italy*

[2]*IMEM-CNR, Parco Area delle Scienze 37/A, 43124 Parma, Italy*

[3]*Dipartimento di Chimica, GIAF Università di Parma, Parco Area delle Scienze 17/A 43124 Parma, Italy*

[4]*Dipartimento di Fisica, Università di Firenze, via Sansone 1, 50019 Sesto Fiorentino (FI), Italy*

[5]*Istituto Sistemi Complessi-CNR, via Madonna del Piano 10, 50019 Sesto Fiorentino (FI), Italy*

[6]*IMM-CNR, via Gobetti 101, 40129 Bologna, Italy*

[7]*Institute Laue-Langevin, Boîte Postale 156, F-38042, Grenoble, France*

(Received 16 October 2012; revised manuscript received 24 June 2013; published 30 July 2013)

We report on the synthesis and characterization of $BiFe_{0.5}Mn_{0.5}O_3$, a potential type-I multiferroic compound displaying temperature-induced magnetization reversal. Bulk samples were obtained by means of solid-state reaction carried out under the application of hydrostatic pressure of 6 GPa at 1100 °C. The crystal structure is a highly distorted perovskite with no cation order on the *B* site, where, besides a complex scheme of tilt and rotations of the TM-O_6 octahedra, large off-centering of the bismuth ions is detected. Below $T_1 = 420$ K the compound undergoes a first weak ferromagnetic transition related to the ordering of iron-rich clusters. At lower temperatures (just below RT) a complex thermally activated mechanism induces at first an enhancement of the magnetization at $T_2 = 288$ K, then a spontaneous reversal giving rise to a negative response. The complementary use of powder neutron diffraction, superconducting quantum interference device magnetometry, and Mössbauer spectroscopy allowed us to propose as a possible interpretation of the overall magnetic behavior the presence of an uncompensated competitive coupling between nonequivalent clusters of weakly ferromagnetic interactions characterized by different critical temperatures and resultant magnetizations.

DOI: 10.1103/PhysRevB.88.014431 PACS number(s): 75.85.+t, 75.60.Jk, 76.80.+y, 75.30.Et

I. INTRODUCTION

The members of the $BiFe_{1-x}Mn_xO_3$ solid solution are potentially multiferroic materials, displaying different structural, magnetic, and electric properties depending on the x value. Both the end members of the series ($x = 0, 1$) are widely studied, due to the presence of multiferroic properties with above room-temperature ordering temperatures. $BiFeO_3$ crystallizes in a distorted perovskite structure with $R3c$ rhombohedral symmetry related to the presence of ferroelectric properties. Antiferromagnetism is detected, ascribed to the cycloidal rotation of a spin-canted magnetic structure.[1] On the other hand $BiMnO_3$ is an orbital-order-induced ferromagnet with ordering temperature around 100 K.[2,3] The accurate determination of its crystallographic structure is a matter of debate, in particular for what concerns the presence of the inversion center; indeed at present the existence of ferroelectricity in $BiMnO_3$ is still under investigation.[4,5] Surprisingly, the members of the Fe/Mn solid solution are poorly studied in bulk form,[6–9] despite the observation of interesting chemical and physical properties. The most intriguing phenomenon reported so far for the compounds with $0.25 < x < 0.5$ is the so-called spontaneous magnetization reversal (MRV). In several ferrimagnets, as predicted by Néel,[10] MRV occurs caused by the presence of two different temperature dependences of sublattice magnetizations arising from magnetic ions at nonequivalent crystallographic sites,[11–18] while the presence of disorder on the perovskite *B* site as, for instance, in $YFe_{0.5}Cr_{0.5}O_3$[19] and $(La_{1-x}Bi_x)Fe_{0.5}Cr_{0.5}O_3$,[20] together with Dzyaloshinskii-Moriya (DM) interaction gives rise to MRV due to uncompensated weak ferromagnetism involving clusters of nonequivalent exchange interactions. For what concerns $BiFe_{0.5}Mn_{0.5}O_3$, the current explanations of the phenomenon ascribe the process to a thermally activated competition between DM interaction and single-ion anisotropy[6] (a hypothesis that is not strengthened by sufficient experimental confirmations), or to an extrinsic process due to the presence of inhomogeneities.[9] In order to clarify the nature of the MRV in the system, we performed Mössbauer measurements on a 48% ^{57}Fe-enriched $BiFe_{0.5}Mn_{0.5}O_3$ sample, together with accurate structural analyses and magnetization measurements, whose results are presented in this work. The performed study yields experimental support to a mechanism which is at least coexistent (if not alternative) to the previously hypothesized ones. It is shown that the MRV is ascribable to the competitive coupling of iron- and manganese-rich regions characterized by different exchange interactions, resultant magnetizations, and critical temperatures.

II. EXPERIMENT

Polycrystalline $BiFe_{0.5}Mn_{0.5}O_3$ was synthesized via a solid-state reaction carried out in high-pressure, high-temperature conditions, using a Walker-type multianvil press. The starting powder binary oxides (Bi_2O_3, Fe_2O_3, Mn_2O_3) in stoichiometric amounts were ground together and encapsulated in gold foils. The best thermodynamic synthesis conditions were determined as 6 GPa of isotropic pressure, 1100 °C, and 1.5 h of reaction time. The sample was quenched to room temperature before pressure was slowly released.

Powder x-ray diffraction (XRD) patterns were collected using Cu $K\alpha$ radiation on a Thermo ARL X'tra powder diffractometer equipped with a Thermo Electron Si(Li) solid-state detector to eliminate the incoherent background produced

by the florescence of Fe and Mn. Data collections were performed by 0.01°–0.02° steps with counting times ranging from 3 to 10 s.

Single-crystal XRD data were collected with Mo $K\alpha$ radiation on a Bruker AXS Smart diffractometer, equipped with an APEX II CCD area detector.

Electron diffraction (ED) and high-resolution electron microscopy (HREM) were carried out using a Philips Tecnai F20 transmission electron microscope operating at 200 kV. The specimens were prepared by grinding the powders in isopropyl alcohol and evaporating the suspension on a copper grid covered with a holey carbon film.

Powder neutron-diffraction data were collected at the D1B and D2B beamlines of the Institut Laue-Langevin in Grenoble. Experiments were performed in the 10–500 K temperature range, with incident beam wavelengths 2.52 and 1.59 Å. All the refinements were carried out using the GSAS package.[21,22]

Magnetic measurements were performed, operating only in standard dc mode, by using a superconducting quantum interference device (SQUID) magnetometer MPMS-XL. The instrument allows the control of both temperature (between 5 and 680 K) and magnetic field intensity (from 0 to 5 T). Supplementary magnetic measurements were performed at higher temperatures (up to 850 °C) by using a DSM8 stationary pendulum magnetometer.

Mössbauer measurements were performed by means of a Wissel spectrometer, calibrated by using a standard metal iron foil, and an Oxford flux cryogenic system with a base temperature of 1.8 K. The source was a 25 mCi ^{57}Co in rhodium matrix with Lamb-Mössbauer factor $f_s = 0.63$, as measured by applying the method described in Ref. 23. Twenty-two spectra were collected between 67.8 and 300 K in the absence of applied field: four of them above the higher critical MRV temperature $T_2 = 288$ K (as explained in detail in the text), five between T_2 and $T_3 = 250$ K, which is the second critical MRV temperature, five others from T_3 to the compensation temperature at 10 Oe ($T^* = 186$ K) and finally, eight spectra under T^*. Since we were interested in evaluating the magnetic components of the spectra, by mixing 48% ^{57}Fe enriched active material powder with Boron nitride as excipient we prepared a high-t_a sample, containing 22.08 mg/cm^2 of compound.

III. RESULTS

A. Structural analysis

Preliminary single-crystal XRD experiments were initially performed on different samples. In all cases most of the observed reflections could be indexed on the basis of an orthorhombic perovskite superstructure with $a = 5.5728(5) \approx \sqrt{2}a_p$, $b = 11.2065(10) \approx 2\sqrt{2}a_p$, and $c = 15.7430(15)$ Å $\approx 4a_p$, 16 times in volume with respect to the fundamental pseudocubic perovskitic cell with lattice parameter a_p. However, additional weaker satellites were typically observed in single-crystal patterns, suggesting the presence of a larger pseudocubic superstructure with $a \approx b \approx c \approx 4a_p$. A careful analysis pointed out that the relative intensity of the satellites varies from sample to sample, suggesting a twinning phenomenon at the origin of these weaker reflections. This agrees with the results of powder

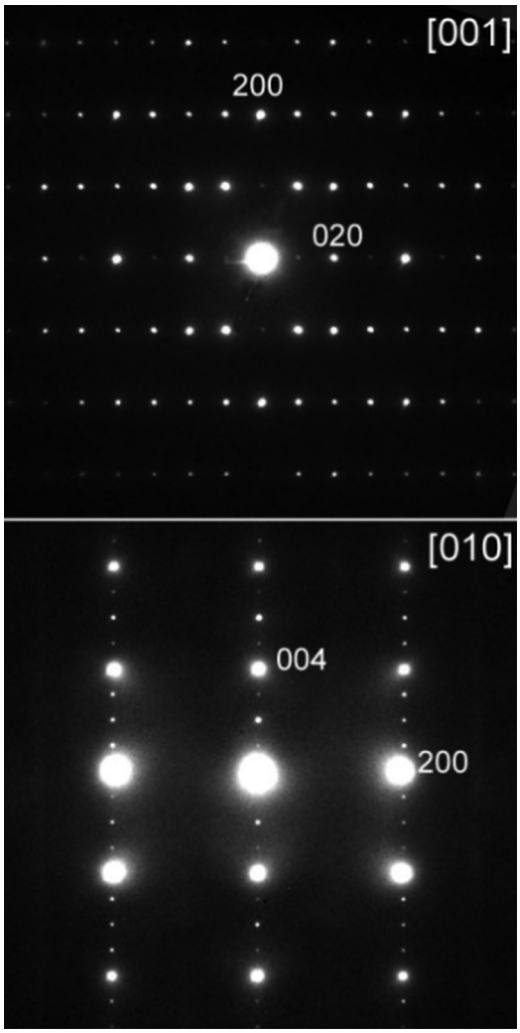

FIG. 1. SAED patterns taken on single-domain regions of $BiFe_{0.5}Mn_{0.5}O_3$ samples.

XRD, reported as Supplemental Material in Fig. 1,[24] where, besides the reflections indicating the presence of the sole extra phase of Bi_2CO_5 in amounts of a few percent, no extra peaks were observed by indexing the pattern with the orthorhombic cell. A definitive confirmation was offered by TEM experiments, indicating the orthorhombic lattice as the true cell of the structure. Selected area electron-diffraction (SAED) patterns taken along the fundamental [001] and [010] zone axes of the orthorhombic cell are shown in Fig. 1. The existence of short-scale twinning involving the exchange of the fundamental perovskite axes (quite similar by the metrical point of view) was clearly evidenced by high-resolution electron microscopy (HREM) coupled with SAED, the data and their accurate analysis being reported in Fig. 2. Different crystals were analyzed by single-crystal XRD in order to identify a "single-domain" sample, but all the examined crystals having suitable dimensions were found to be more or less affected by twinning. In order to solve and refine the structure intensities, data were collected from the crystal showing the lowest twinning contribution. The structure was solved using SIR2004 (Ref. 25) in the *Pnam* space group and refined with SHELX97 (Ref. 26) making use of anisotropic

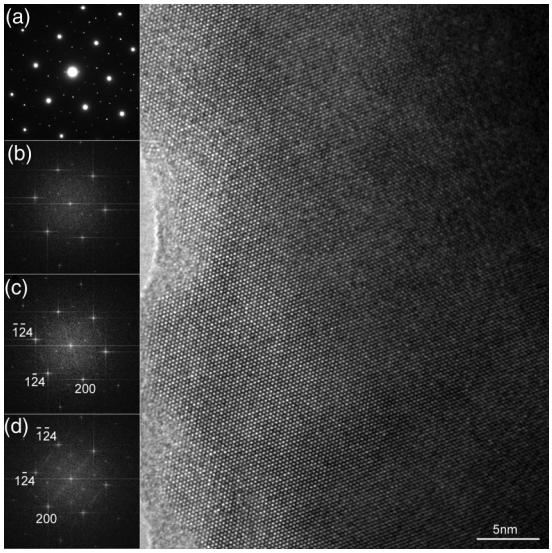

FIG. 2. HREM image taken in a [111] projection of the fundamental perovskite structure showing the presence of twinning domains involving a 60° rotation of the orthorhombic superstructure lattice around the zone axis. The corresponding experimental SAED pattern is shown in inset (a), compared with the fast Fourier transform (FFT) obtained on the whole as well as on the upper and lower regions of the image reported in the insets (b)–(d), respectively; (c) and (d) patterns are indexed on the basis of the orthorhombic superstructure. The "composite" experimental SAED pattern can be explained on the basis of twinning domains evidenced by the corresponding HREM image and its fast Fourier transform.

thermal parameters for all atoms. The transition metal sites, TM1 and TM2, were refined by constraining the occupancy of both Mn and Fe to 50%, in agreement with the observed equivalence of their average bond distances. Owing to the presence of residual twinning contributions to the observed intensities, the agreement indices obtained in the refinement are not optimal, but the description of the structure can be considered completely reliable, as confirmed by the Rietveld refinement of the powder diffraction data, produced by using the structural parameters determined by single-crystal XRD. Crystal data and refined parameters are reported in Table I (and Table I in the Supplemental Material[24]), while selected cation-oxygen bond lengths are gathered in Table II. The cation-oxygen bond lengths evidence large distortions of the coordination around the bismuth atoms, induced by the strong stereochemical activity of the $6s^2$ lone pair. It is noteworthy that this effect involves also the iron/manganese coordination octahedra, which appear to be largely distorted and consequently high values of the corresponding quadrupolar splitting are expected (for Fe ions $Q_s = 0.65$ mm/s). In spite of this the two TM sites show, as previously pointed out, the same average bond distance, confirming the absence of cation ordering. Analysis of the TM-O distances in terms of charge distribution was performed using the program CHARDIS99,[27] suggesting the exclusive presence of Fe^{3+} and Mn^{3+} within the structure (see Table II). The charge distribution method implemented in CHARDIS99 is a development of the bond-valence approach, allowing a more reliable treatment of atomic charges in solid solutions and structures with distorted coordinations. A representation of the crystal structure projected along the [001] and [100] directions is reported in Fig. 3.

The large superstructure observed in $BiFe_{0.5}Mn_{0.5}O_3$ is quite unusual, as most of the known orthorhombic double perovskites display a crystallographic cell with $a \approx b \approx \sqrt{2}a_p$, $c \approx 2a_p$ related to the tilt of the BO_6 octahedra. The large periodicity is ascribed to the distortions produced by the bismuth atoms inducing a complex structure where the TMO_6 octahedra are both tilted along the c direction, with TM-O-TM bond angles ranging from 157.6° to 146.2°, and rotated in the ab plane with a $+\ +\ -\ -$ scheme[28] along c. It is noteworthy that the displacement scheme of the bismuth ions involves the formation of dimers that are consistent with an antiferroelectric structure, as shown in Fig. 4.

TABLE I. Crystal data and refined parameters.

	Pnam			Reflections collected	16500
	$a = 5.5728(5)$ Å			Data/restraints/parameters	1356/0/97
	$b = 11.2065(10)$ Å			Goodness of fit on F^2	1.249
Space group	$c = 15.7430(15)$ Å			R indices $[I > 4\sigma(I)]$	$R_1 = 0.0561$, $wR_2 = 0.1291$
Unit cell dimensions	983.175(3) Å^3			R indices (all data)	$R_1 = 0.0641$, $wR_2 = 0.1249$
Volume	X	Y	Z	site occupancy factor	U_{eq} (Å^2)
Bi1	0.27114(17)	0.13754(8)	$\frac{3}{4}$	1	0.0105(2)
Bi2	0.71523(18)	−0.12525(8)	$\frac{3}{4}$	1	0.0107(2)
Bi3	0.72410(16)	−0.12533(6)	0.51022(5)	1	0.0189(2)
TM1[a]	0.7429(4)	0.12118(19)	0.62580(14)	1	0.0082(5)
TM2[a]	0.74827(4)	−0.37683(19)	0.62344(14)	1	0.0055(5)
O1	0.680(3)	0.0769(18)	$\frac{3}{4}$	1	0.0144(4)
O2	0.578(2)	−0.2236(11)	0.6307(8)	1	0.013(3)
O3	0.723(4)	0.1638(16)	0.5057(9)	1	0.035(4)
O4	−0.032(2)	0.2473(11)	0.8433(8)	1	0.010(2)
O5	0.484(3)	0.0052(14)	0.5977(9)	1	0.021(3)
O6	0.971(3)	−0.0198(15)	0.6134(10)	1	0.025(4)
O7	0.815(4)	−0.3877(19)	$\frac{3}{4}$	1	0.020(4)

[a]Site occupancy factors of both Mn and Fe (TM1 and TM2) fixed to 0.50.

TABLE II. List of relevant bond distances (Å).

TM1-O4	1.952(13)	TM2-O6	1.939(16)	Bi1-O4	2.242(13)	Bi2-O7	2.240(3)	Bi3-O2	2.339(13)
TM1-O3	1.955(15)	TM2-O2	1.966(13)	Bi1-O4	2.243(13)	Bi2-O1	2.27(3)	Bi3-O3	2.395(18)
TM1-O5	1.993(16)	TM2-O5	1.988(15)	Bi1-O1	2.378(18)	Bi2-O2	2.308(13)	Bi3-O5	2.414(16)
TM1-O6	2.038(16)	TM2-O7	2.030(15)	Bi1-O4	2.554(13)	Bi2-O2	2.308(13)	Bi3-O6	2.435(17)
TM1-O1	2.048(14)	TM2-O3	2.089(14)	Bi1-O4	2.554(13)	Bi2-O6	2.838(17)	Bi3-O5	2.458(16)
TM1-O4	2.179(14)	TM2-O2	2.156(13)	Bi1-O7	2.81(3)	Bi2-O6	2.838(17)	Bi3-O3	2.54(3)
				Bi1-O5	3.059(15)	Bi2-O7	2.99(3)	Bi3-O6	3.053(17)
				Bi1-O5	3.059(15)	Bi2-O5	3.090(16)	Bi3-O3	3.12(3)
				Bi1-O1	3.24(3)	Bi2-O5	3.090(16)	Bi3-O4	3.176(13)
				Bi1-O6	3.245(17)	Bi2-O2	3.238(13)	Bi3-O2	3.218(13)
				Bi1-O1	3.245(17)	Bi2-O2	3.238(13)	Bi3-O3	3.241(18)
				Bi1-O1	3.364(17)	Bi2-O7	3.350(3)	Bi3-O4	3.423(13)
Avg.	2.028(14)	Avg.	2.028(14)	Avg.	2.833(18)	Avg.	2.817(19)	Avg.	2.818(17)
$Q(ij)$[a]	3.11	$Q(ij)$	3.03	$Q(ij)$	2.88	$Q(ij)$	2.73	Q(ij)	3.07

[a] $Q(ij)$s are the cationic charges as computed by CHARDIS99 (Ref. 27).

Surprisingly, if one considers the dramatically different structures of the two end members of the $BiFe_{1-x}Mn_xO_3$ solid solution, the structure observed here is very close to the one reported in Ref. 7 for $BiFe_{0.75}Mn_{0.25}O_3$, in particular for what concerns the scheme of both octahedral distortions and bismuth ion shifts. Within this framework the observation of similar physical properties in $BiFe_{0.5}Mn_{0.5}O_3$ and $BiFe_{0.75}Mn_{0.25}O_3$ suggests a strong relation between the structure and the complex physical properties of this family of compounds.

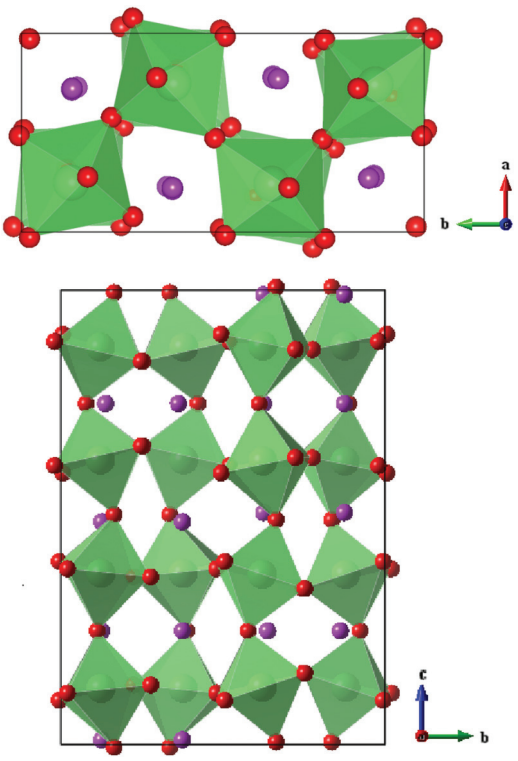

FIG. 3. (Color online) $BiFe_{0.5}Mn_{0.5}O_3$ crystal structure projected on the *ab* (top) and *bc* (bottom) planes made using the program VESTA (Ref. 35). The vertex-sharing light green octahedra are linked by the red oxygen atoms, while the purple spheres represent the bismuth ions.

High-resolution neutron-diffraction data were collected at 10, 310, and 500 K allowing a thorough refinement of the structural features of the system which points out the absence of symmetry changes in the whole investigated temperature range. Two phases, namely $BiFe_{0.5}Mn_{0.5}O_3$ and Bi_2CO_5, in a 20:1 ratio, were necessary to index the patterns. Rietveld plots of the refinements performed at 500 and 10 K are reported in Fig. 5. Thanks to the high-resolution data collected at 500 K it was possible to study the sample in its paramagnetic phase confirming the goodness of the previously proposed structural model. In particular, due to the difference in atomic scattering factors of the iron and manganese ions in neutron diffraction, it was possible to exclude the presence of *B*-site cation ordering. The 10 K data show the raising of purely magnetic peaks with $k = (0\ 0\ 0)$ propagation vector related to antiferromagnetic *G*-type magnetic ordering of the *B*-site transition metals. The spin arrangement is shown in Fig. 6 and involves collinear atomic moments along the *a* direction, with zero component

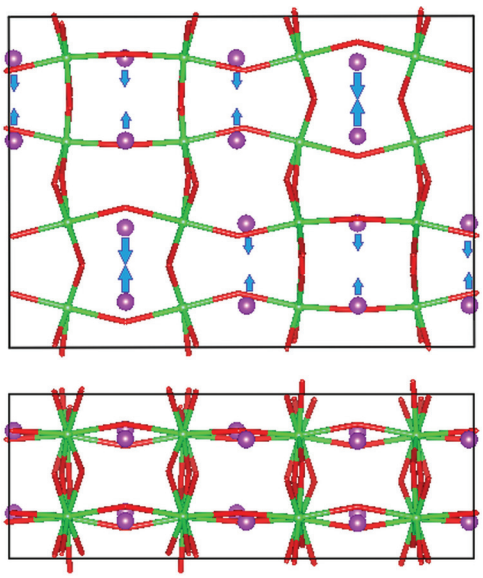

FIG. 4. (Color online) Relative shifts of the bismuth ions in the crystal structure of $BiFe_{0.5}Mn_{0.5}O_3$ projected on the *bc* (top) and *ac* (bottom) plane.

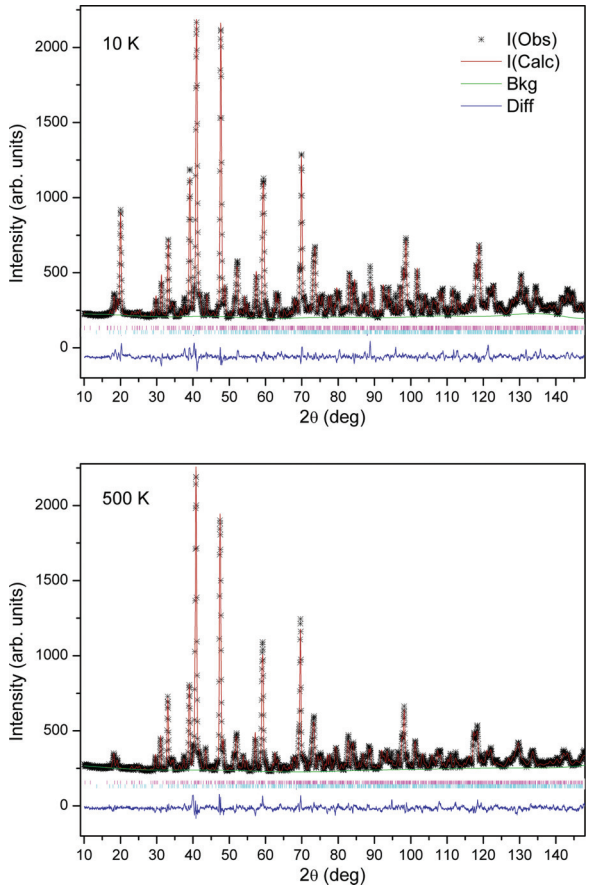

FIG. 5. (Color online) Rietveld refinements of the neutron diffraction patterns collected at 500 and 10 K (bottom and top, respectively).

along b and c, and the presence of isotropic first neighborhood antiferromagnetic interactions. The observed atomic moment is 5.1 μ_B, slightly higher than the expected one (4.5 μ_B) for an

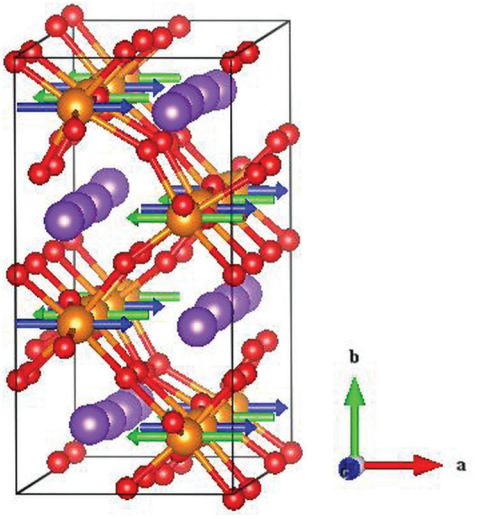

FIG. 6. (Color online) Magnetic structure of $BiFe_{0.5}Mn_{0.5}O_3$: In orange are represented the transition metal ions, in purple the bismuth ones, and in red oxygen. The blue and green arrows indicate the antiferromagnetic atomic moments.

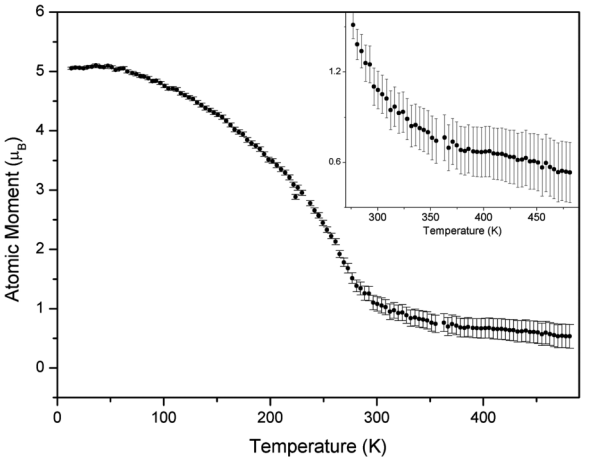

FIG. 7. Refined atomic moment in the 10–500 K range. The inset shows the 280–450 K region, where short-range magnetic interactions are detected.

averaged structure containing high-spin Fe^{3+} and Mn^{3+} ions, indicating that the magnetic structure at 10 K is long-range ordered and clearly shows the absence of inhomogeneities involving the magnetic structure and sizable spin fluctuations.

The high-flux data collected at D1B between 10 and 500 K allowed accurate study of the magnetic structure thermal evolution. No spin reorientations as well as changes in the propagation vector were observed in the whole examined temperature range. Figure 7 reports the refined atomic moment as a function of temperature, showing a Brillouin-like behavior up to about 290 K and suggesting the loss of long-range magnetic correlation to be located at this temperature. However, a weak and broad signal, observed in the 2θ regions where the magnetic reflections are detected, persists up to about 400 K, indicating the presence of small clusters of magnetically ordered TM ions. A similar behavior, as well as G-type spin structure, was previously observed in $YFe_{1-x}Mn_xO_3$, being ascribed to short-range magnetic ordering.[29]

The thermal evolution of the lattice parameters, reported in Fig. 8, shows an appreciable anisotropic behavior. Differently from a, that shows a linear behavior at high temperatures,

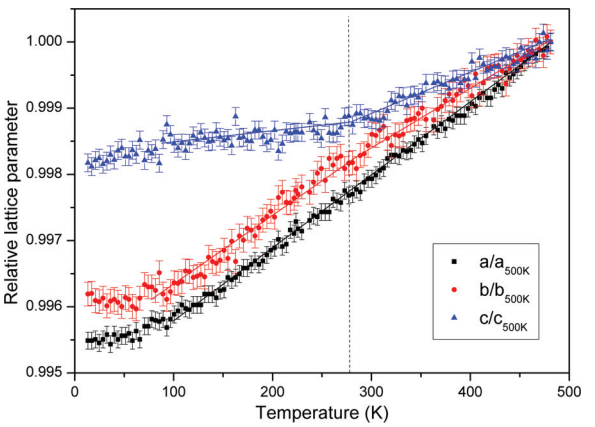

FIG. 8. (Color online) Lattice parameter variation as a function of temperature. Solid lines are guides to the reader's eye. The dashed vertical line indicates the long-range magnetic ordering temperature.

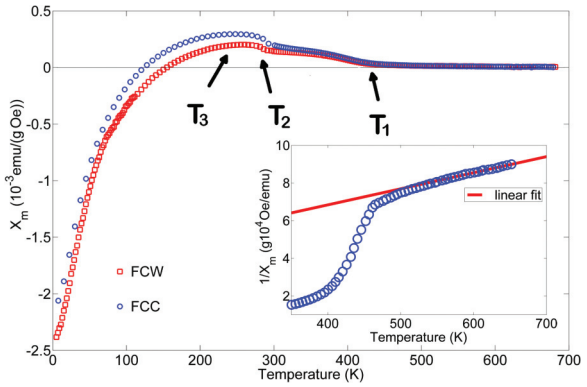

FIG. 9. (Color online) $BiFe_{0.5}Mn_{0.5}O_3$ mass susceptibility measured with applied field $H = 100$ Oe, using Field-Cooled Cooling (FCC) and Field-Cooled Warming (FCW) procedures.

both the b and c parameters display anomalies at 288 K, i.e., the long-range magnetic ordering temperature; the anomalies consist in opposite sign slope variations, slight for b but noticeable for c, suggesting the presence of spin-lattice coupling, which could be indicative of magnetoelectric effects.

B. Magnetic characterization

Field-Cooled (FC) magnetometry was performed between 5 and 680 K with applied field $H = 100$ Oe on an as-grown pellet. The measurements, recorded both on cooling and warming, are reported in Fig. 9. The sample shows a primary paramagnetic-to-weak ferromagnetic transition at $T_1 = 420$ followed at lower temperature by a complex mechanism composed by two interconnected phenomena taking place at $T_2 = 288$ K and $T_3 = 250$ K, finally leading to MRV. High-temperature measurements aimed at the study of the paramagnetic region of the compound were performed with applied field $H = 10$ kOe, due to the weak magnetic signal of the sample and are reported in the inset of Fig. 9. The fitting of the linear region of the inverse susceptibility curve (above T_1) allowed us to determine the Curie-Weiss temperature $\theta = -400$ K, revealing a global antiferromagnetic nature of the interactions, and a number of Bohr magnetons per formula unit corresponding to 5.4 μ_B. This value is consistent if compared to the expected value 5.2 μ_B for high-spin Fe^{3+} (5.9 μ_B) and Mn^{3+} (4.9 μ_B). The observed weak ferromagnetic signal between T_1 and T_2 can be ascribed to a second-order mechanism allowed by the low symmetry of the system and producing spin canting, as, for example, single-ion anisotropy or antisymmetric DM interaction. Just below room temperature the low-field susceptibility undergoes a two-step transition (see Fig. 9): At T_2 antiferromagnetic long-range order takes place and below T_3 a complex thermal mechanism leads the system at first to a compensation ($\chi = 0$) and then to a remarkable negative response. On the contrary, high-field measurements do not show the same mechanism of compensation and at T_3 the transition disappears, suppressed by the applied magnetic field, as shown as Supplemental Material in Fig. 2.[24] This suggests the interactions leading to MRV to be very weak, in agreement with the hypothesis of weak ferromagnetism induced by a second-order mechanism. In a recent paper,[9] the reversal of magnetization in $BiFe_{1-x}Mn_xO_3$ ($x = 0.3, 0.4$) is considered an extrinsic process due to the presence of inhomogeneities related to the observation of exchange bias in the hysteresis loop and the absence of MRV, if the system is field cooled below T_N (T_2 in this case). Wide magnetic characterizations we performed are in contrast with these results, as resumed in Figs. 3 and 4 in the Supplemental Material.[24]

$M(H)$ measurements performed at 300, 280, 240, 100, and 5 K are reported in Figs. 10(a) and 10(b). The hysteresis loops were measured starting from 5 up to -5 T after a field cooling in low magnetic field. All the collected data show that the high-field magnetization trend is typical of an antiferromagnetic (AFM) system; however, in the low-field regime two different behaviors, taking place below and above T_3, respectively, can be discriminated. At higher temperatures the hysteresis is generated by the weak ferromagnetic component and gives rise to a small remanent magnetization (0.012 emu/g), that could be explained by the presence of mesoscopic structures (clusters) of spin-canted domains. Below T_3, the coercive field

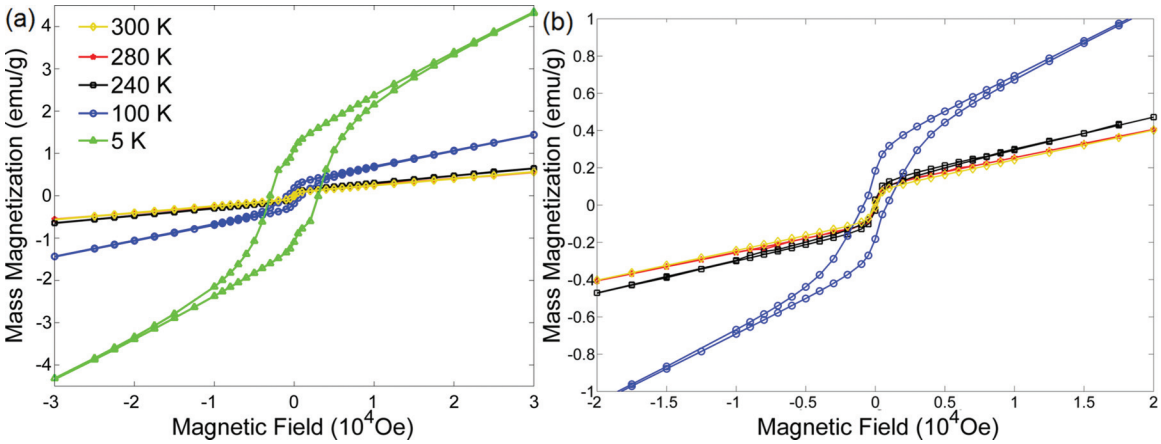

FIG. 10. (Color online) (a) Hysteresis loops measured at different temperatures from RT to 5 K across the reversal process thermal thresold. At 5 K a complex kinked shape is detected. (b) Hysteresis loops at 100, 240, 280, and 300 K were highlighted. At low temperature is clearly observed the presence of a sensible stricture in the central part of the curve possibly indicating the superimposition of two different magnetic contributions.

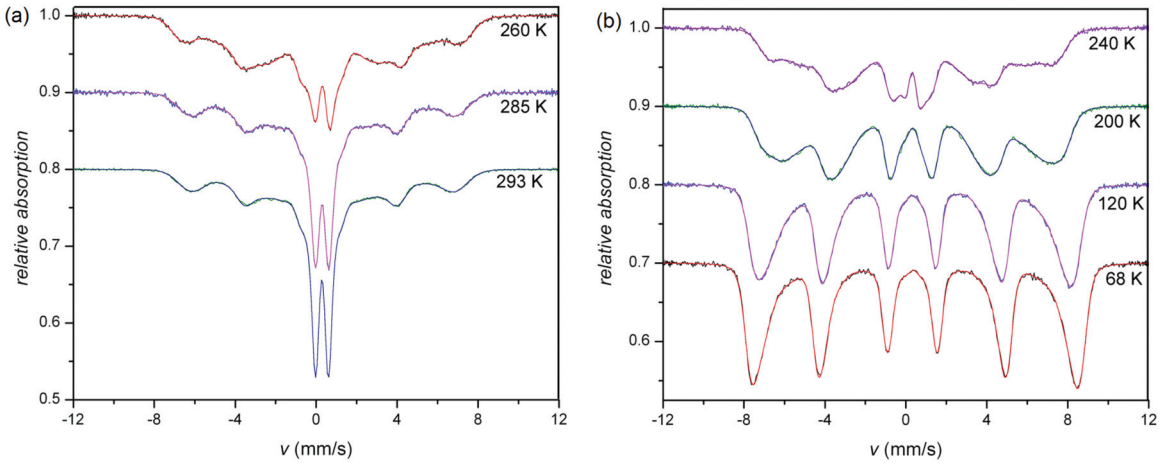

FIG. 11. (Color online) Mössbauer spectra collected (a) above and (b) below T_3.

and spontaneous magnetization increase and the hysteresis loop starts opening out, showing a complex shape, which is probably due to the coexistence of two different weak ferromagnetic contributions [see the blue circles in Fig. 10(b)], whose competition is possibly responsible for MRV. At 5 K the presence of two symmetrical kinks [Fig. 10(a)] suggests for the two components a "soft" and a "hard" character, respectively.

Another remarkable characteristic of the $M(H)$ curves is the increase, below T_3, of the high-field susceptibility by decreasing the temperature. Even if quite unusual for magnetically ordered compounds, this behavior could be expected for systems where MRV originates from the competition of two independent magnetic components with different exchange constants, the weaker dominating at lower temperature. The obtained value of remanent magnetization at 5 K is 0.062 μ_B/f.u., consistent with a spin-canted system, while the coercive field is 3000 Oe.

C. Mössbauer characterization

Mössbauer spectra collected at different temperatures in the range 293–68 K are reported in Figs. 11(a) and 11(b). At high T values, spectra are marked by a saturated, winged doublet, which arises from an unsaturated magnetic structure, extending from -8 to $+8$ mm/s, corresponding to hyperfine fields ≈45 T. By decreasing the temperature, the progressive disappearance of the wells between the magnetic lines indicates the growing of medium field components (≈25 T), rising from the simultaneous fall of the doublet intensity: Around $T = T_3$ the external lines are flat and the depth of the doublet lines is comparable to that of the magnetic lines.

A further decrease of T affects the line shape making the external lines to become well defined again, suggesting a falloff in the medium field components [see Fig. 11(b)]. Therefore, the evolution of the Mössbauer cross section is described by means of a doublet (sub-5) and four magnetic components, characterized by Gaussian field distributions, which lead to sextets of Voigt profiles.[30,31] One of them (sub-4) is used to fit the wings of the doublet and it should be considered as that part of the superparamagnetic-like component which takes into account inhomogeneous and/or homogeneous effects. The three remaining magnetic structures describe the magnetically ordered part of the cross sections; namely, sub-3 describes the medium field component and a strong hyperfine mean field variation starting around 230 K, and the last two (sub-2 and sub-1) are necessary to outline the high-field components, since the low-temperature spectra show asymmetric external lines. All of these subspectra are also able to take into account inhomogeneous broadenings of the electric parameters, i.e., quadrupolar splitting and isomer shift, by means of an additional Gaussian distribution, whose linewidth returns to values lower than $2\Gamma_N = 0.2$ mm/s. The electric parameters of the magnetic sextet used to fit the wings of the doublet were obviously constrained to the same values of sub-5 component. The fitting procedure was performed using the transmission integral method, where the reduced f_s factor was estimated throughout additional pulse height analysis measurements.[23] The obtained RT values for the chemical shift of all the subspectra are in the 0.25–0.35 mm/s range; as far as the quadrupolar splitting is concerned, the doublet and the associated magnetic component have $Q_s = 0.65$ mm/s while all the other magnetic subspectra have $Q_s < 0.30$ mm/s. Moreover, for what concerns subspectrum 4, the angle between the hyperfine field direction and the principal axis of the electric field gradient tensor is ≈0.8 rad. The obtained parameters for $T = 68$, 120, 200, 240, 285, and 293 K are reported in Table III, and the data confirm that the iron oxidation state is 3+. All the fields but sub-4 grow by decreasing T. Sub-1 can be associated to the high-temperature order of the system preexistent at $T > T_2$, while sub-2 interprets the low-temperature magnetic transition since it shows a discontinuity in its contribution to the total Mössbauer thickness and in the hyperfine mean field at T_2, as shown in Fig. 12(a). Moreover around T_3, where the mechanism of reversal is thermally activated, the plot shows a substantial quenching of the sub-3 thickness contribution and a maximization of the sub-2 one. The temperature dependence of the Gaussian broadenings for all the magnetic subspectra is illustrated in Fig. 12(b). Subspectrum 4 is characterized by the highest relative variation and a Gaussian broadening close to the mean field value at 230 K. The Gaussian broadenings of the other components are of the order of few teslas and they decrease smoothly with T, making the spectral lines sharper.

TABLE III. Mössbauer parameter values at selected temperatures: Standard deviations for free parameters are reported in parentheses. $\delta(i)$: center shift of subspectrum (i) with respect to ^{57}Co/Rh source; δ: center shift of the spectrum; $Q_s(i)$: quadrupolar splitting of subspectrum (i); $B_{hyp}(i)$: mean value of the hyperfine magnetic field related to subspectrum (i); $\theta_B(i)$: polar angle of $B_{hyp}(i)$ with respect to the electric field gradient frame; $t_a(i)$: contribution of subspectrum (i) to the total Mössbauer thickness; t_a: total Mössbauer thickness; $\sigma_\delta(i)$: standard deviation value for the inhomogeneous Gaussian distribution of electric parameters related to subspectrum (i); $\sigma_B(i)$: standard deviation value for the Gaussian distribution of hyperfine magnetic field centered on $B_{hyp}(i)$.

T (K)	χ^2	δ (mm/s)	t_a	i	$\delta(i)$ (mm/s)	$Q_s(i)$ (mm/s)	$B_{hyp}(i)$ (T)	$\theta_B(i)$	$t_a(i)$	$\sigma_\delta(i)$ (mm/s)	$\sigma_B(i)$ (mm/s)
68	1189	0.400	12.7	1	0.387(3)	0.150(4)	50.56(4)		4.0(8)	0.18(1)	1.2(1)
				2	0.403(3)	0.166(5)	48.0(4)		5.(1)	0.19(1)	2.3(2)
				3	0.417(9)	0.20(2)	43.0(8)		2.9(4)	0.19(1)	5.3(3)
				4	0.39(3)	0.65	16.6(5)	0.84(8)	0.51(3)	0.15(2)	4.8(6)
				5	0.39	0.65			0.06(1)	0.15	
120	1079	0.384	12.3	1	0.363(4)	0.113(9)	49.20(7)		2.5(4)	0.15(1)	1.55(8)
				2	0.389(3)	0.185(6)	46.5(2)		5.5(9)	0.22(1)	2.8(2)
				3	0.398(6)	0.19(1)	41.(1)		3.5(7)	0.18(1)	5.1(5)
				4	0.35(3)	0.65	17.9(8)	0.80(9)	0.67(7)	0.15(3)	8.(1)
				5	0.35	0.65			0.08(3)	0.15	
200	1055	0.350	11.5	1	0.303(9)	0.02(2)	46.7(1)		1.1(2)	0.14(2)	2.0(1)
				2	0.353(3)	0.171(8)	41.8(7)		5.3(8)	0.20(1)	4.0(2)
				3	0.347(7)	0.200(2)	34.(1)		3.(1)	0.22(1)	4.1(8)
				4	0.366(1)	0.65	23.(2)	0.84(3)	2.2(5)	0.18(1)	8.(1)
				5	0.366	0.65			0.25(2)	0.18	
240	1009	0.328	11.0	1	0.297(7)	0.05(2)	44.26(8)		1.5(1)	0.18(2)	2.6(2)
				2	0.337(6)	0.21(1)	34.8(5)		5.6(8)	0.21(1)	6.5(4)
				3	0.38(5)	0.24(9)	23.6(7)		0.3(2)	0.1(1)	3.(1)
				4	0.325(6)	0.64(1)	17.(4)	0.79(4)	3.0(9)	0.13(1)	10.(2)
				5	0.325	0.64			0.53(7)	0.13	
260	989	0.309	10.6	1	0.285(7)	0.04(2)	42.9(1)		1.9(3)	0.20(2)	3.1(2)
				2	0.318(8)	0.17(1)	30.7(6)		4.7(8)	0.20(1)	7.(1)
				3	0.296(4)	0.18(6)	22.6(7)		0.4(4)	0.3(1)	2.(2)
				4	0.312(4)	0.658(6)	13.(1)	0.81(4)	2.2(5)	0.16(1)	6.(1)
				5	0.312	0.658			1.4(1)	0.16	
285	1004	0.297	9.9	1	0.289(7)	0.08(1)	40.3(1)		2.57(7)	0.16(1)	4.0(1)
				2	0.31(2)	0.18(4)	31.0(4)		0.5(3)	0.16(1)	2.4(6)
				3	0.32(1)	0.13(3)	22.6(7)		2.1(7)	0.04(4)	5.(1)
				4	0.291(2)	0.632(4)	9.(1)	0.81(4)	2.1(4)	0.13(1)	6.0(8)
				5	0.291	0.632			2.64(5)	0.13	
293	1221	0.296	9.9	1	0.281(4)	0.089(7)	40.4(1)		2.2(1)	0.15(1)	3.78(7)
				2	0.38(3)	0.24(4)	31.5(3)		0.3(2)	0.11(6)	2.9(7)
				3	0.323(9)	0.18(2)	22.3(6)		2.7(4)	0.	8.(1)
				4	0.28(1)	0.63(9)	7.1(5)	0.82(3)	1.3(2)	0.10(7)	4.2(4)
				5	0.283(1)	0.632(1)			3.37(9)	0.109(2)	

The magnetic fields distributions are derived from the parameters reported in Figs. 12(a) and 12(b) and they are illustrated in Figs. 13(a) and 13(b) for selected temperatures distinguished by strong and weak superparamagnetic-like components, respectively. In correspondence with the high-fields region the high-T distributions are characterized by a peak emerging from a flat trend. By lowering T the distributions become double peaked and finally they tend to collapse into a single peak. The main feature in the line-shape thermal evolution concerns the contribution to the total Mössbauer thickness due to the superparamagnetic-like doublet with its wings (sub-5 and sub-4), which decreases exponentially with T from 50% at room temperature to a practically negligible percentage under 200 K. The contribution of the superparamagnetic-like doublet $[t_a(4) + t_a(5) = t_{spar}]$, normalized to the total thickness t_a, is illustrated in Fig. 14 and it shows a discontinuity between 180 and 200 K. The thermal trend of t_{spar} was fitted by the following exponential function:

$$y_0 + ae^{-\frac{\Delta}{T-T_C}}, \tag{1}$$

above and below the discontinuity. For $T \leqslant 180$ K, we obtained $\Delta \approx 460$ K and $T_C = 0$; for $T \geqslant 200$ K, $\Delta \approx T_C \approx 170$ K. It is noteworthy that 460 K is rather close to the primary canted antiferromagnetic transition temperature T_1. In both cases, the fitted value of a is very close to 1 and this result is a fingerprint that the states that give rise to the superparamagnetic component of the spectra have the same multiplicity of those giving rise to the magnetic ordered components.

A second element to be noted in the Mössbauer spectra thermal evolution regards the hyperfine field mean values of

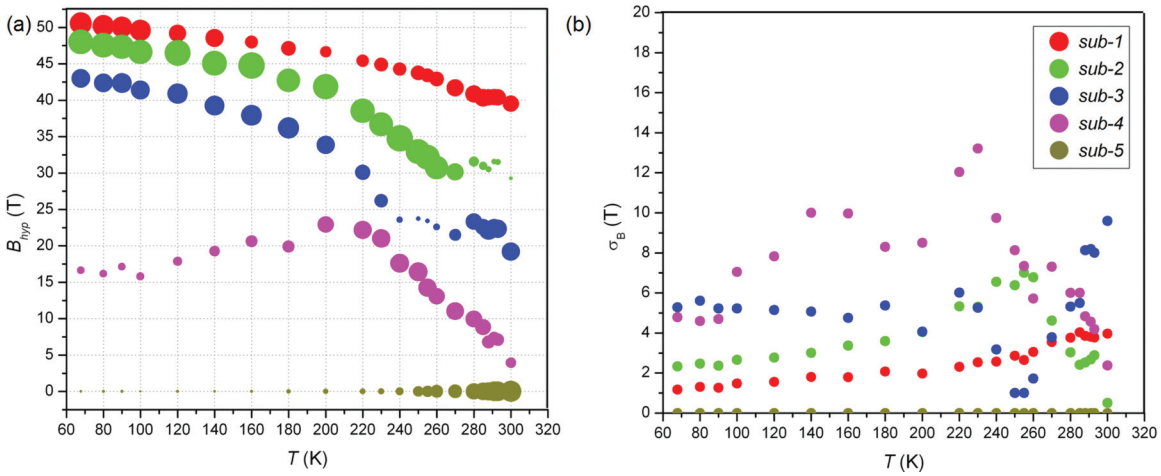

FIG. 12. (Color online) (a) Thermal trend of magnetic hyperfine mean fields for the five subspectra (the areas of the dots are proportional to the corresponding Mössbauer thicknesses). (b) Gaussian width of the magnetic field distributions vs T. The legend refers to both graphics.

the sub-1 component, the relative thickness of which is almost 20% of the total thickness over 200 K. Although its values are a few teslas smaller, the thermal trend of $B_{\mathrm{hyp}}{}^{(1)}$ follows the one of $BiFeO_3$[32,33] suggesting that the respective transition temperatures are likely to be close to each other.

IV. DISCUSSION

The synergic use of crystallographic, magnetic, and Mössbauer characterizations allowed the comprehension of the complex magnetic behavior in $BiFe_{0.5}Mn_{0.5}O_3$. The structural data give the fundamental starting point: the iron and manganese ions are disordered at the perovskites B site, and the analysis of the bond lengths, of the paramagnetic portion of the $1/\chi$ curve, and the iron quadrupolar splitting and isomer shift suggest both the transition metals to be in 3 + oxidation state. The magnetic structure is long-range G-type AFM, therefore all the exchange interactions (Fe-Fe, Fe-Mn, Mn-Mn) are antiferromagnetic, as confirmed by the largely negative Curie-Weiss temperature observed. As a consequence the weakly ferromagnetic moment detected (0.062 μ_B/f.u. at 5 K) should be ascribed to a second-order interaction giving rise to spin canting as, for example, DM interaction or single-ion anisotropy. This is not surprising as several ABO_3 perovskite structures with trivalent A ions and B = iron, chromium, manganese, and their solid solutions often show DM-induced weak ferromagnetism as, for example, the parent compound $BiFeO_3$, where spiral magnetic ordering is observed.[34] Within this framework, the lack of weak ferromagnetic components in the collected neutron-diffraction patterns is due to the sensitivity of the technique, not allowing the detection of signals lower than 0.5 μ_B per magnetic ion. The key for the interpretation of the magnetic behavior is given by the Mössbauer data, showing at 300 K the presence of an ordered component (about 20% of the iron atoms) characterized by high hyperfine field values, together with partially ordered states and a superparamagnetic-like doublet, which shows exponential decreases of its contribution to the thickness as the temperature decreases. Therefore, each iron ion is able to win the superexchange interactions and to take

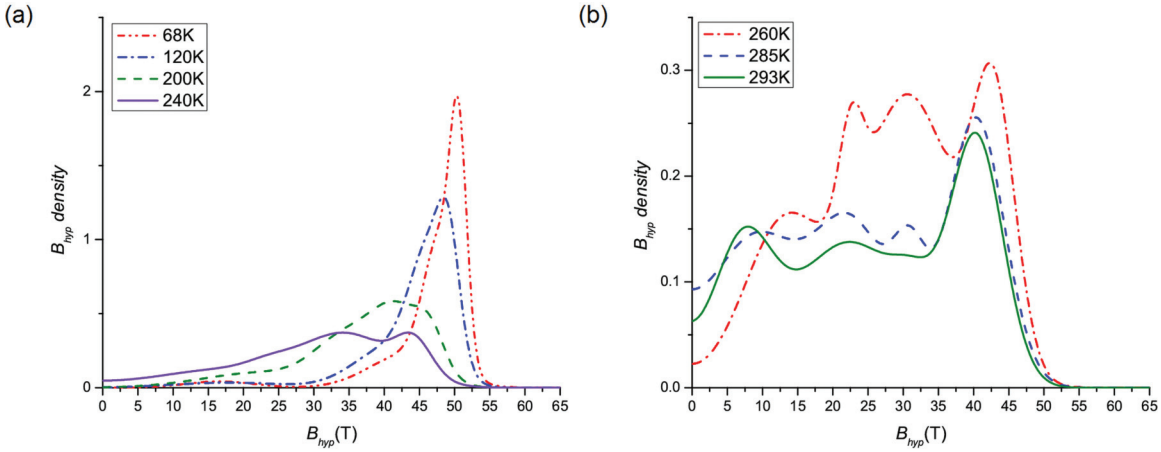

FIG. 13. (Color online) Hyperfine magnetic field density at selected temperatures in the low (a) and high (b) T ranges, corresponding to strong and weak superparamagnetic-like components. The different scales for the vertical axis reflect the collapse of the superparamagnetic-like structure.

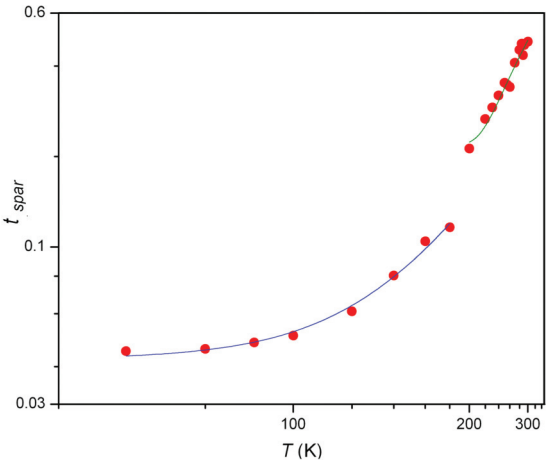

FIG. 14. (Color online) Thermal trend of t_{spar}, normalized to the total thickness t_a, fitted by exponential functions.

on a superparamagnetic behavior by receiving energy from the thermal bath that changes from 170 to 460 K as the system is cooled below 200 K. The MRV occurs in a T range where t_{spar} experiences very significant variations connected to corresponding changes of the thermal populations of the superparamagnetic-like states. Therefore, the interpretation of the magnetization inversion process should take into account the thermal evolution of the superparamagnetic-like component of the Mössbauer spectra. We suggest that by decreasing T the condensation of the superparamagnetic-like states into magnetically ordered ones initially occurs, possibly assisting the incoming Mn long-range order that later goes on without such constraint. Since $BiFeO_3$ and $BiMnO_3$ display very different magnetic ordering temperatures (643 and 100 K, respectively), it is likely to consider that also in a disordered solid solution the iron- and manganese-rich regions may order at different temperatures, the first of them giving rise to the Mössbauer sub-1 component [Fig. 12(a)]. This interpretation also agrees with the broad and weak signal observed in neutron diffraction above the ordering temperature T_2, suggesting the presence of short-range magnetically ordered diffraction domains. Since above $T_1 = 420$ K the compound is paramagnetic, the 420–288 K magnetic behavior is ascribed to a confined G-type antiferromagnetic spin arrangement affected by spin-canted weak ferromagnetism, involving solely the Fe-rich clusters. At T_2 the long-range magnetic ordering involving both Fe and Mn takes place, driven at first by the preordered iron-rich clusters [sub-2 of Fig. 12(a)], and is observed in the magnetization measurements as an increase of the preexistent weak ferromagnetic component. However, by decreasing the temperature, the Fe-Mn interactions, which are dominant from a statistical point of view in the equimolar solid solution, become competitive with the preexistent component and, being evidently connected to a spin canting in the opposite direction, give rise to compensation at T_3 and then to spontaneous reversal of the magnetization. Noteworthy is the fact that the observation of the reversal process is always related to the initial orientation at RT of the small resultant moment of the iron-rich clusters. Indeed in the FC measurements the application of a field forces the weak ferromagnetic component of the ordered clusters to align to positive values; by lowering the temperature the remaining iron ions start to condense into ordered states, assisted by the manganese ones, finally developing negative magnetization.

V. CONCLUSIONS

The use of structural characterization techniques, magnetization measurements, and Mössbauer spectroscopy allowed the meticulous study of the fundamental properties of $BiFe_{0.5}Mn_{0.5}O_3$ in bulk form, making a likely description of the unusual spontaneous (MRV) phenomenon observed in this potentially magnetoelectric compound. The structural characterizations point out that $BiFe_{0.5}Mn_{0.5}O_3$ crystallizes in an orthorhombic perovskite superstructure with $a \approx \sqrt{2}a_p$, $b \approx 2\sqrt{2}a_p$, $c \approx 4a_p$. No cation ordering involving Fe^{3+} and Mn^{3+} is observed and the large distortion of the perovskite lattice is due to a complex scheme of tilt and rotations of the TM-O_6 octahedra together with an extended path of displacements of the bismuth ions yielding an antiferroelectric arrangement. Taking into account the disordered nature of the $BiFe_{0.5}Mn_{0.5}O_3$ solid solution, a mechanism able to describe the MRV process has been developed on the basis of Mössbauer, magnetic, and neutron-diffraction measurements. Basing on the completely different ordering temperatures of the solid solution end members, the mechanism implies, by decreasing the temperature, a composition-dependent progressive ordering of clusters (revealed as antiferromagnetic G-type by neutron diffraction) that starts with the iron-rich ones and then extends to the whole solid. The presence of a weak ferromagnetic component can be ascribed to spin canting, whereas the MRV is ascribed to the fact that the Fe-Mn interactions, statistically dominant but taking place at lower temperatures, produce a ferromagnetic component which orders antiparallel to the preexistent one. It is quite interesting to note that the structural characterization pointed out anomalies in the thermal dependence of the lattice parameters occurring at the magnetic long-range ordering temperature T_2, indicating a spin-lattice coupling that could be indicative of magnetoelectric effect.

ACKNOWLEDGMENTS

Fondazione Cariparma is thanked for financial support. Ente Cassa di Risparmio di Firenze is thanked for its financial support (Contract No. 2010.0419). The authors acknowledge the Institute Laue-Langevin (Grenoble, France) for providing technical and financial support.

*Corresponding author: davide.delmonte@fis.unipr.it

[1]G. Catalan and J. F. Scott, Adv. Mater. **21**, 2463 (2009).

[2]T. Kimura, S. Kawamoto, I. Yamada, M. Azuma, M. Takano, and Y. Tokura, Phys. Rev. B **67**, 180401 (2003).

[3]N. A. Hill and K. M. Rabe, Phys. Rev. B **59**, 8759 (1999).

[4]T. Atou, H. Chiba, K. Ohoyama, Y. Yamaguchi, and Y. Syono, J. Solid State Chem. **145**, 639 (1999).
[5]V. Goian, S. Kamba, M. Savinov, D. Nuzhnyy, F. Borodavka, P. Vaněk, and A. A. Belik, J. Appl. Phys. **112**, 074112 (2012).
[6]P. Mandal, A. Sundaresan, C. N. R. Rao, A. Iyo, P. M. Shirage, Y. Tanaka, C. Simon, V. Pralong, O. I. Lebedev, V. Caignaert, and B. Raveau, Phys. Rev. B **82**, 100416 (2010).
[7]A. A. Belik, A. M. Abakumov, A. A. Tsirlin, J. Hadermann, J. Kim, G. Van Tendeloo, and E. Takayama-Muromachi, Chem. Mater. **23**, 4505 (2011).
[8]M. Azuma, H. Kanda, A. A. Belik, Y. Shimakawa, and M. Takano, J. Magn. Magn. Mater. **310**, 1177 (2007).
[9]A. A. Belik, Inorg. Chem. **52**, 2015 (2013).
[10]L. Néel, Ann. Phys. (Leipzig) **3**, 137 (1948).
[11]E. W. Gorter and J. A. Schulkes, Phys. Rev. **90**, 487 (1953).
[12]R. Pauthenet, J. Appl. Phys. **29**, 253 (1958).
[13]S. I. Ohkoshi, T. Iyoda, A. Fujishima, and K. Hashimoto, Phys. Rev. B **56**, 11642 (1997).
[14]S. I. Ohkoshi, Y. Abe, A. Fujishima, and K. Hashimoto, Phys. Rev. Lett. **82**, 1285 (1999).
[15]K. Yoshii, A. Nakamura, Y. Ishii, and Y. Morii, J. Solid State Chem. **162**, 84 (2001).
[16]K. Yoshii, J. Solid State Chem. **159**, 204 (2001).
[17]V. A. Khomchenko, I. O. Troyanchuk, R. Szymczak, and H. Szymczak, J. Mater. Sci. **43**, 5662 (2008).
[18]Y. L. Su, J. C. Zhang, Z. J. Feng, L. Li, B. Z. Li, Y. Zhou, Z. P. Chen, and S. X. Cao, J. Appl. Phys. **108**, 013905 (2010).
[19]Nagamalleswararao Dasari, P. Mandal, A. Sundaresan, and N. S. Vidhyadhiraja, Europhys. Lett. **99**, 17008 (2012).
[20]K. Vijayanandhini, C. Simon, V. Pralong, Y. Bréard, V. Caignaert, B. Raveau, P. Mandal, A. Sundaresan, and C. N. R. Rao, J. Phys.: Condens. Matter **21**, 486002 (2009).
[21]A. C. Larson and R. B. Von Dreele, Los Alamos National Laboratory Report No. LAUR 86-748 (2000).
[22]H. B. Toby, J. Appl. Cryst. **34**, 210 (2001).
[23]G. Spina, E. Pugliese, L. Cianchi, F. Del Giallo, M. Lantieri, and P. Moretti, J. Phys. Conf. Ser. **217**, 012015 (2010).
[24]See Supplemental Material at http://link.aps.org/supplemental/10.1103/PhysRevB.88.014431 for details concerning the structural analysis, high-field FC magnetic characterization and experimental study on the proposed (Ref. 9) extrinsic nature of MRV.
[25]M. C. Burla, R. Caliandro, M. Camalli, B. Carrozzini, G. L. Cascarano, L. De Caro, C. Giacovazzo, G. Polidori, and R. Spagna, J. Appl. Cryst. **38**, 381 (2005).
[26]G. M. Sheldrick, SHELXL97, Program for the crystal structure refinement (University of Gottingen, Germany, 1993).
[27]M. Nespolo, G. Ferraris, and H. Ohashi, Acta Crystallogr. B **55**, 902 (1999).
[28]A. M. Glazer, Acta Crystallogr. B **28**, 3384 (1972).
[29]P. Mandal, C. R. Serrao, E. Suard, V. Caignaert, B. Raveau, A. Sundaresan, and C. N. R. Rao, J. Solid State Chem. **197**, 408 (2013).
[30]J. Puerta and P. Martin, Appl. Opt. **20**, 3923 (1981).
[31]D. G. Rancourt, Nucl. Instr. Methods Phys. Res., Sect. B **44**, 199 (1989).
[32]D. Kothari, V. Raghavendra Reddy, A. Gupta, C. Meneghini, and G. Aquilanti, J. Phys.: Condens. Matter **22**, 356001 (2010).
[33]V. S. Pokatilov, A. S. Sigov, and A. O. Konovalova, Bull. Russ. Acad. Sci.: Phys. **74**, 347 (2010).
[34]J. Wang, J. B. Neaton, H. Zheng, V. Nagarajan, S. B. Ogale, B. Liu, D. Viehland, V. Vaithyanathan, D. G. Schlom, U. V. Waghmare, N. A. Spaldin, K. M. Rabe, M. Wuttig, and R. Ramesh, Science **299**, 1719 (2003).
[35]K. Momma and F. Izumi, J. Appl. Crystallogr. **44**, 1272 (2011).